ADVANCED ENERGY MATERIALS

www.advenergymat.de

Highly Efficient Tandem Organic Solar Cell Enabled by Environmentally Friendly Solvent Processed Polymeric Interconnecting Layer

Kai Zhang, Baobing Fan, Ruoxi Xia, Xiang Liu, Zhicheng Hu, Honggang Gu, Shiyuan Liu, Hin-Lap Yip, Lei Ying, Fei Huang,* and Yong Cao*

In the field of organic solar cells (OSCs), tandem structure devices exhibit very attractive advantages for improving power conversion efficiency (PCE). In addition to the well researched novel pair of active layers in different subcells, the construction of interconnecting layer (ICL) also plays a critical role in achieving high performance tandem devices. In this work, a new way of achieving environmentally friendly solvent processed polymeric ICL by adopting poly[(9,9-bis(3′-(*N*,*N*-dimethylamino)propyl)-2,7-fluorene)-alt-5,5′-bis(2,2′-thiophene)-2,6-naphthalene-1,4,5,8-tetracaboxylic-*N*,*N*′-di(2-ethylhexyl)imide] (PNDIT-F3N) blended with poly(ethyleneimine) (PEI) as the electron transport layer (ETL) and PEDOT:PSS as the hole transport layer is reported. It is found that the modification ability of PNDIT-F3N on PEDOT can be linearly tuned by the incorporation of PEI, which offers the opportunity to study the charge recombination behavior in ICL. At last, tandem OSC with highest PCE of 12.6% is achieved, which is one of the best tandem OSCs reported till now. These results offer a new selection for constructing efficient ICL in high performance tandem OSCs and guide the way of design new ETL materials for ICL construction, and may even be integrated in future printed flexible large area module device fabrication with the advantages of environmentally friendly solvent processing and thickness insensitivity.

Organic solar cells (OSCs) based on organic materials offer specific advantages such as low cost, light weight, solution processable, and mechanical flexible.[1–4] After decades of development in material design, remarkable progress in power conversion efficiency (PCE) have been achieved by virtue of the attainment of extending light absorption spectrum and enhancing the light absorption intensity of active layers.[5–10] However, the performance of OSCs still inferior to other photovoltaic technologies due to several intrinsic defects (e.g., the thermalization losses of high energy photons and the transmission losses of low energy photons). To overcome these intrinsic losses of OSCs and enhance the PCE, one promising approach is adopting tandem structure. This type of device has two or more subcells stacked in series with complementary light absorption spectrum, in which the thermalization losses can be reduced by the utilization of high energy photons in front cell with wide-bandgap active layer and the transmission losses can be reduced by the utilization of low energy photons in back cell with narrow-bandgap active layer.[11–14] Thus, both the high energy and low energy photos can be utilized to generate photocurrent. Generally, the open-circuit voltage (V_{oc}) of tandem OSC should be the sum of subcells's V_{oc}, while the short-circuit current density (J_{sc}) is restricted by the minimum J_{sc} of subcells.[15–18] Thus, another striking advantage of tandem structure OSCs is that it exhibits a relatively low photocurrent and thus is favorable for achieving efficient large area module OSCs, since the power loss on the series resistance in large area electrode (can be simply expressed by Ohm's law, $P_R = I^2R_s$, where the I is current while R_s is the series resistance) will be obviously suppressed due to the lower photocurrent.[19–22]

To achieve high performance tandem OSCs, much effort has been dedicated to the rational molecular design of materials with complementary absorption spectrum that are suitable for high performance subcell active layer.[23–25] Thanks to the significant progress of recently emerged nonfullerene acceptors with easily tunable absorption spectra, more complementary spectrum of both subcells can be obtained by utilizing nonfullerene-based active layer, and very promising tandem OSCs have been achieved.[26,27]

In addition to the attentively researched novel pair of active layers in different subcells, the construction of interconnecting layer (ICL) also plays a critical role in achieving high performance tandem device. In general, the ICL is composed of a hole

Dr. K. Zhang, B. Fan, R. Xia, X. Liu, Dr. Z. Hu, Prof. H.-L. Yip, Prof. L. Ying, Prof. F. Huang, Prof. Y. Cao
Institute of Polymer Optoelectronic Materials and Devices
State Key Laboratory of Luminescent Materials and Devices
South China University of Technology
Guangzhou 510640, P. R. China
E-mail: msleiying@scut.edu.cn; msfhuang@scut.edu.cn
Dr. H. Gu, Prof. S. Liu
State Key Laboratory of Digital Manufacturing Equipment and Technology
Huazhong University of Science and Technology
Wuhan 430074, P. R. China
The ORCID identification number(s) for the author(s) of this article can be found under https://doi.org/10.1002/aenm.201703180.

DOI: 10.1002/aenm.201703180

transport layer (HTL) and electron transport layer (ETL) pair which should provide Ohmic contact with both subcells for the charge extraction and recombination.[28–30] Another important criterion for ICL is its compatibility for future printed large area device.[31–33] The ICL should be processed from environmentally friendly solvent at low temperature and be able to provide good solvent resistance for the bottom subcell to protect it from being eroded by following subcell solution. Currently, nearly all of the high performance tandem OSCs were realized with ICL containing the n-type metal oxide combined with the p-type metal oxide or p-type polymer,[34] such as ZnO/PEDOT:PSS,[35,36] ZnO/CuSCN,[37] and ZnO/conjugated polymers.[26,27,38] Although these combinations resulted in excellent device performances, the inorganic metal oxides may suffer from several intrinsic weaknesses. For example, it was reported that the high annealing temperature and inorganic nature of metal oxides may hinder their application in flexible or wearable OSCs (e.g., exfoliation when bending device).[36] In addition, in some cases the n-type metal oxides are degraded by photoetching, and device stability will be reduced.[39,40] Under such circumstances, organic/organic ICLs can be an ideal option to address these problems. Unfortunately, there are only a few works reported on this topic. Kippelen's group and Jang's group reported the use of polymeric ICL to construct inverted tandem OSCs and obtained a PCE of 8.2% and 8.91% respectively.[41,42] Yang's group achieved a tandem OSCs with PCE of 10.1% by adapting a relatively complicated polyelectrolyte 1/polyelectrolyte 2/PEDOT:PSS trilayer structure.[43] Chang's group demonstrated flexible tandem OSC with PCE of 9.2% employing all organic ICL.[44] These pioneer contributions proved the feasibility of using solution processed organic/organic ICL for flexible tandem OSCs.

In this work, we demonstrate an new way of achieving water/alcohol processed polymeric ICL for conventional tandem OSCs by adopting poly[(9,9-bis(3′-(*N*,*N*-dimethylamino)propyl)-2,7-fluorene)-alt-5,5′-bis(2,2′-thiophene)-2,6-naphthalene-1,4,5,8-tetracaboxylic-*N*,*N*′-di(2-ethylhexyl)imide] (PNDIT-F3N) blended with poly(ethyleneimine) (PEI) as the ETL and PEDOT:PSS as the HTL. This new ICL can successfully protect the front cell from being eroded by back cell solutions. It is found that the modification ability of PNDIT-F3N on PEDOT can be linearly tuned by the incorporation of PEI, which offers us an ideal model to study the charge recombination behavior in ICL. Moreover, efficient ICL with excellent charge recombination property with ICL thickness varied from 60 to 140 nm are obtained. The front cell is constructed with a novel wide-bandgap conjugated polymer poly((4,8-bis(5-((2-ethylhexyl)thio)thiophen-2-yl)benzo[1,2-*b*:4,5-*b*′]dithiophene-2,6-diyl)-*alt*-2-(3-ethylheptyl)-6-octyl-[1,2,3]triazolo[4,5-*f*]isoindole-5,7(2*H*,6*H*)-dione) (PSTzBI-EHp), which presents a PCE of 9.2% when blending with $PC_{71}BM$. The back cell consists of a narrow-bandgap conjugated polymer consist of thienyl-substituted benzo[1,2-*b*:4,5-*b*′]dithiophene unit and alkoxycarbonyl-substituted thieno[3,4-b]thiophene unit (PBDTTT-E-T) and a nonfullerene acceptor, 2,2′-((2Z,2′Z)-((5,5′-(4,4,9,9-tetrakis(4-hexylphenyl)-4,9-dihydros-indaceno[1,2-b:5,6-b′]dithiophene-2,7-diyl)bis(4-((2-ethylhexyl)-oxy)thiophene-5,2-diyl))bis(methanylylidene))-bis(3-oxo-2,3-dihydro-1H-indene-2,1-diylidene))dimalononitrile (IEICO), which presents long-wavelength absorbance that is complementary with the front cell. The combination of such two subcells using the newly developed ICL leads to a tandem OSC with highest PCE of 12.6% (measured to be 13.2% without aperture), which is one of the best tandem OSCs that reported as far as we know. This result is comparable to tandem OSCs with inorganic metal oxides ICL, and offers a new selection for constructing efficient ICL in high performance tandem OSCs. This ICL with specific advantages of environmentally friendly solvent processing and thickness insensitivity exhibits great potential in future printed flexible large area module device, and provides a new guideline for the rational design of organic ICL.

The chemical structures of the materials used in this work and tandem device structure are shown in **Figure 1**a,b. The novel wide-bandgap polymer PSTzBI-EHp used as the front cell active layer is optimized from our reported wide-bandgap donor–acceptor type conjugated polymer PTzBI,[45] which shows improved solubility and slightly higher V_{oc} when blending with $PC_{71}BM$. As shown in Figure 1c, the main absorption range of PSTzBI-EHp:$PC_{71}BM$ (1:1, w/w) for the front cell covers the range from 300 to 710 nm, which is complementary with the absorption spectrum of PBDTTT-E-T:IEICO (1:1.2, w/w)[46] for the back cell that covers a broad range from 300 to 920 nm, demonstrating that the constructed tandem OSCs can effectively harvest solar photon in a wide range. To identify the dependence of photovoltaic performances on thickness of novel PSTzBI-EHp:$PC_{71}BM$, we initially evaluated the device based on PSTzBI-EHp with configuration of ITO/PEDOT:PSS/PSTzBI-EHp:$PC_{71}BM$/PNDIT-F3N/Ag, where the active layer thickness varied from 70 to 170 nm. Detailed device data are shown in Figure S1 and Table S1 of the Supporting Information. For the device with 70 nm active layer, a PCE of 8.7% was achieved. When the thickness increased to 90 nm, a best PCE of 9.2% with J_{sc} of 13.5 mA cm^{-2}, V_{oc} of 0.93 V, and fill factor (FF) of 73% was achieved (**Figure 2**a). However, further increasing the active layer thickness to 170 nm resulted in a decreased PCE of 7.6%, this can be ascribed to the increased charge recombination as the thickness increasing.[47] By contrast, for the back cell based on PBDTTT-E-T:IEICO, a PCE of 9.6% with J_{sc} of 17.5 mA cm^{-2}, V_{oc} of 0.82 V, and FF of 67% was achieved with active layer thickness of 100 nm, which is comparable to the reported value.[26] The J_{sc}s of these devices were verified by external quantum efficiency (EQE) measurement and are shown in Figure 2b and Table S1 (Supporting Information).

We have reported a naphthalene diimide-based water/alcohol soluble polymer PNDIT-F3N as an efficient ETL in both OSCs and perovskite solar cells, and it was found that this ETL can be applied to produce high performance devices in a wide range of thicknesses owing to the good electron transport property of the backbone.[48,49] These features offer the possibility of achieving robust ICL to protect the bottom subcell from being destroyed by following subcell solution. The tandem OSCs with device structure of ITO/PEDOT (40 nm)/front cell (90 nm)/PNDIT-F3N:PEI (*x*:*y*, w/w, 20 nm)/PEDOT (40 nm)/back cell (100 nm)/PNDIT-F3N (10 nm)/Ag (100 nm) were fabricated. Here the thickness of front cell and back cell are temporarily set to be the same as the optimized conditions in single-junction cells. To achieve all solution processed polymeric ICL, we first used PNDIT-F3N/PEDOT as ICL. However, the resulted tandem OSCs exhibited very poor device performance, indeed S-shaped *J*–*V* curves were observed (shown in **Figure 3**a), showed a low PCE with a V_{oc} of 1.28 V. Since both PNDIT-F3N and PEDOT were reported to be excellent ETL and HTL for charge extraction in single junction cells, the

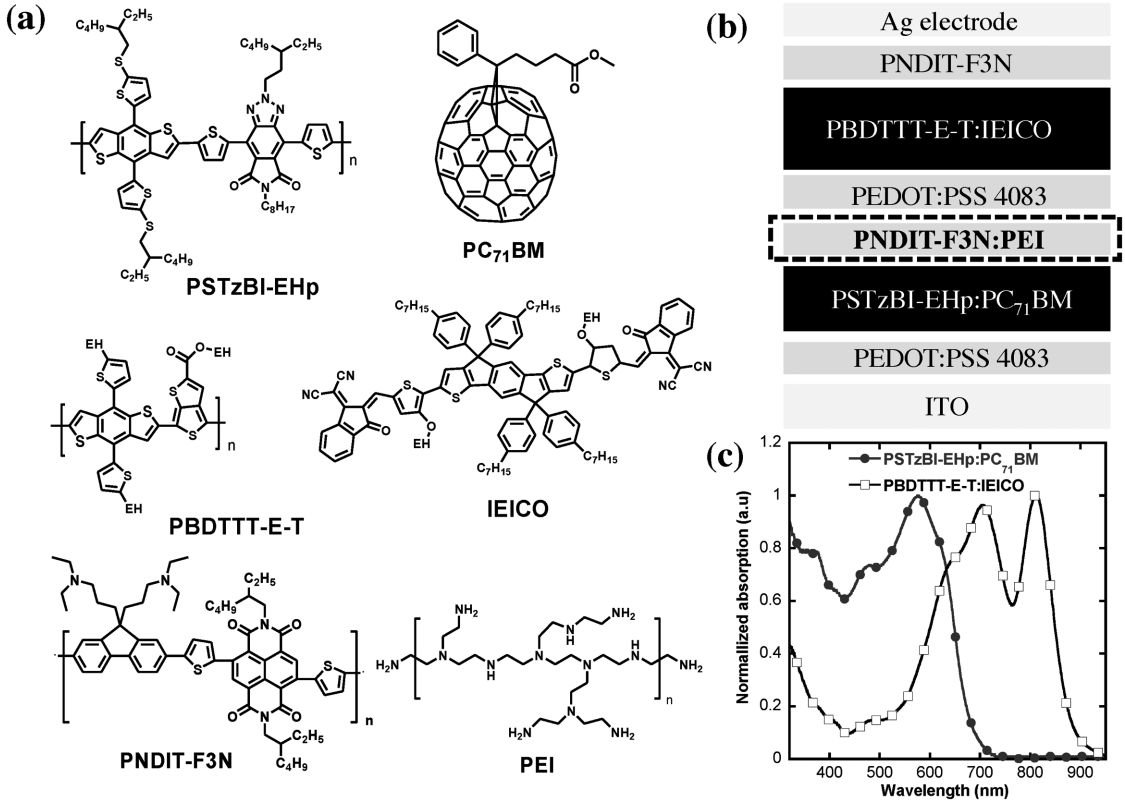

Figure 1. a) Chemical structures of the active layer and interlayer materials used in this study. b) Tandem OSC device structure and c) normalized absorption spectra of the active layers for the front and back cells.

poor performance of tandem cell was suspected result from the poor charge recombination in ICL itself. Interestingly, we found blending PEI into PNDIT-F3N can eliminate the S shape and even result in an efficient tandem OSC. Here PEI was selected as the second component in ICL because the large amount of amine-group on PEI main chain and side chain endowed it the ability to largely reduce the work function (WF) of PEDOT.[50] Moreover, both PNDIT-F3N and PEI (with weight average molecular weight of 10 000 kDa) show excellent methanol solubility but insoluble in water, which offer them the feasibility to be solution processed without being dissolved during the spin-cast of PEDOT. The *J*–*V* curves of the tandem OCSs with different ratio of PNDIT-F3N:PEI-based ICL are shown in Figure 3a and **Table 1**. When a small amount of PEI was blended into PNDIT-F3N (*x*:*y* = 4:1, w/w), the V_{oc} of tandem OSC increased to 1.61 V. Further increasing the blend ratio of PNDIT-F3N:PEI to 3:2, the resulted device was successfully connected in series with V_{oc} equal to the sum of both subcells. The devices also showed a decent FF of 70% and a J_{sc}

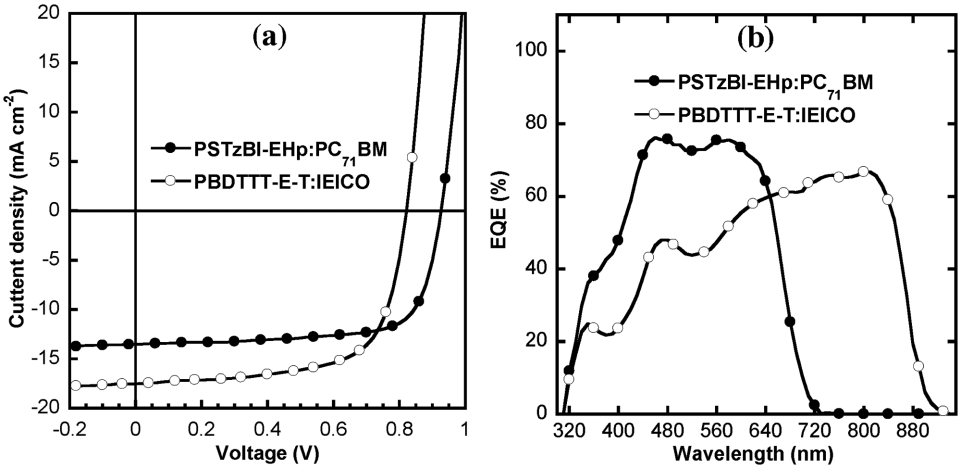

Figure 2. a) *J*–*V* and b) EQE characteristics of wide-bandgap active layer and narrow-bandgap active layer in single junction cells.

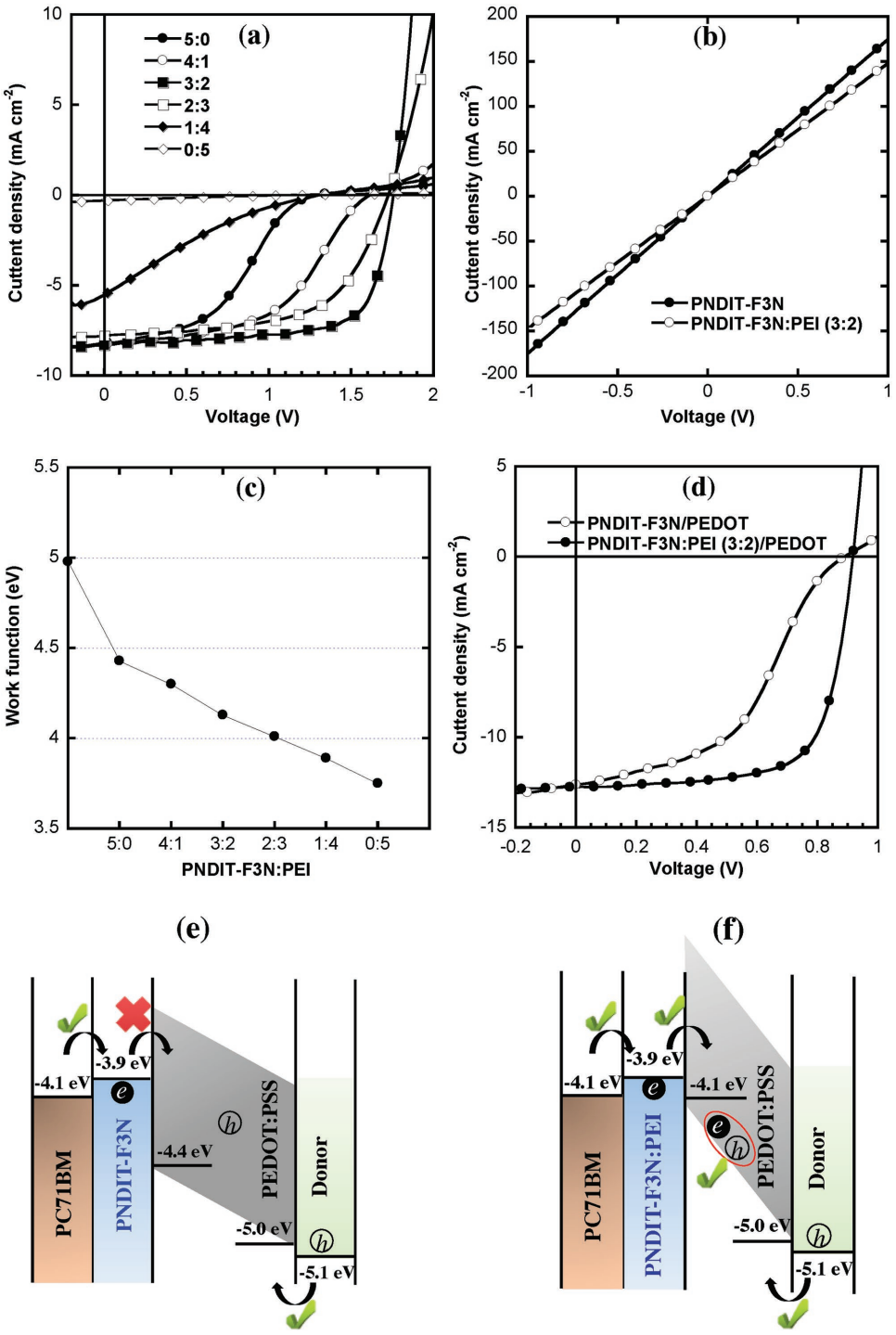

Figure 3. a) *J–V* characteristics of tandem OSCs with ICL contained different ratio of PNDIT-F3N:PEI. b) *J–V* characteristics of Schottky junction devices based on PNDIT-F3N and PNDIT-F3N:PEI (3:2). c) The WF of PEDOT coated with different ratio of PNDIT-F3N:PEI. d) The *J–V* characteristics of equivalent devices ITO/PEDOT/PSTzBI-EHp:$PC_{71}BM$/ETL/PEDOT/Ag with PNDIT-F3N and PNDIT-F3N:PEI (3:2) as ETL. Illustrations of e) charge accumulation in ICL and f) charge recombination in ICL.

of 8.3 mA cm^{-2}, leading to a PCE of 10.2%. However, further increasing the PEI content resulted in a decrease in device performance. In the extreme case, when 20 nm pure PEI was used in the ICL, the device showed nearly no *J–V* characteristics. Since PEI is a completely insulating material, the incorporation of 20 nm PEI would introduce a very large series resistance in the ICL, and therefore electrons are unable to transport from front cell through PEI layer to combine with holes in ICL. Actually, in single-junction cells, the optimal thickness of PEI is precisely controlled within 10 nm.[50] However, in the tandem OSCs,

Table 1. Device data of tandem OSCs with ICL contained different ratio of PNDIT-F3N:PEI.

PNDIT-F3N:PEI (20 nm, *x*:*y*)	J_{sc} [mA cm^{-2}]	V_{oc} [V]	FF [%]	PCE[a] (avg/max) [%]
5:0	8.2	1.28	42	4.0 ± 0.4 (4.4)
4:1	8.3	1.61	49	6.3 ± 0.3 (6.6)
3:2	8.3	1.75	70	9.9 ± 0.3 (10.2)
2:3	7.8	1.73	64	8.4 ± 0.2 (8.6)
1:4	5.5	1.32	22	1.5 ± 0.1 (1.6)
0:5	0.3	1.10	18	0.5 ± 0.2(0.7)

[a]The average data were achieved from ten independent devices.

the introduction of 10 nm pure PEI in the ICL only resulted in mediocre device performance with PCE of 4.6% and V_{oc} of 0.91 V (shown in Figure S2, Supporting Information), suggesting that the ICL was unable to create an efficient recombination junction and resulted in photovoltage loss since 10 nm PEI was not robust enough to prevent PEDOT penetration.

To understand why blend insulating polymer PEI into semiconducting polymer PNDIT-F3N resulting efficient tandem OSCs, the morphology test was carried out by using atomic force microscope. These results are shown in Figure S3 of the Supporting Information. The pure PNDIT-F3N film and PEI film exhibited a very smooth surface with roughness of 0.6 and 0.5 nm, respectively. When PEI was blended into PNDIT-F3N, the surface roughness slightly increased to 4.8 nm (4:1), 5.6 nm (3:2), 5.2 nm (2:3), and 4.5 nm (1:4), which may be favorable for providing better contact between HTL (PEDOT) and ETL (PNDIT-F3N:PEI), and thus facilitate the charge encounter. However, the best performed tandem device was obtained with PNIDT-F3N:PEI ratio of 3:2, demonstrating that morphology change should not be responsible for the device performance improvement. We carried out the conductivity test of PNDIT-F3N blended with or without PEI. PNDIT-F3N and the best performed ratio PNDIT-F3N:PEI (3:2) were selected to fabricate Schottky devices with device structure ITO/PNDIT-F3N:PEI (5:0 and 3:2, 20 nm)/Ag. The *J*–*V* curves are shown in Figure 3b. It can be seen that with the addition of a small amount of PEI into PNDIT-F3N, the conductivity of PNDIT-F3N slightly decreased, but still remained in a reasonable level, implying that the electron transport pathway was not hindered by the addition of small amount of PEI. It also indicated that the variation of conductivity cannot be responsible for the obvious tandem OSC improvement. There must be some other triggers. To further understand what happened in the ICL when PEI was blended into PNDIT-F3N, the WF of PEDOT modified by PNDIT-F3N:PEI (as shown in Figure 3c and Table S2, Supporting Information) was studied. Ag was also included for comparison. Scanning Kelvin probe microscope revealed that the WF of PEDOT and Ag were 4.98 and 4.59 eV, respectively, which agreed with generally reported values.[51] After the modification by PNDIT-F3N, the WF of Ag was reduced to 4.04 eV, which is quite close to the lowest unoccupied molecular orbital (LUMO) level of $PC_{71}BM$ (≈4.1 eV), thus electron was able to be collected by Ag electrode in single junction OSCs.[6,48] However, the WF of PEDOT was slightly reduced to 4.43 eV with the modification of PNDIT-F3N, which meant that there was a big energy barrier between the PNDIT-F3N modified PEDOT and the LUMO of $PC_{71}BM$, the electrons were inefficiently extracted from front cell to recombine with holes that extracted from back cell in ICL. These results can be understood since amine-group was reported to play a key role in determining the WF modification ability of water/alcohol soluble ETL materials.[41,52] In our study, the large amount of amine-group on PEI main chain and side chain endowed it the ability to largely reduce the WF of PEDOT (reduced to 3.75 eV, summarized in Table S2, Supporting Information), however, the relatively low amine content in PNDIT-F3N side chain offered it moderate modification ability on PEDOT (reduced to 4.43 eV, summarized in Table S2, Supporting Information). It is of particular interest to note that the WF of PEDOT can be linearly tuned upon the incorporation of PEI into PNDIT-F3N. As shown in Figure 3c and Table S2 (Supporting Information), the WF of PEDOT was reduced to 4.13 eV with the modification of PNDIT-F3N:PEI (3:2), which is low enough to collect electron from front cell, thus the tandem device with PNDIT-F3N:PEI (3:2) as ETL showed an ideal tandem behavior. To get insight into these results, we compared devices based on PNDIT-F3N and the best performed ratio PNDIT-F3N:PEI (3:2) with device of structure ITO/PEDOT (40 nm)/PSTzBI-EHp:$PC_{71}BM$ (90 nm)/PNDIT-F3N:PEI (5:0 and 3:2, 20 nm)/PEDOT (40 nm)/Ag. Note here the PEDOT/Ag functioned as cathode. The device based on pure PNDIT-F3N showed apparent S shape (shown in Figure 3d), just as the same case in tandem device, which can be ascribed to the low efficient electron extraction from active layer to PEDOT/Ag. However, the device with PNDIT-F3N:PEI (3:2) showed a very typical OSC *J*–*V* curve with V_{oc} of 0.92 V and FF of 70%, implying that electrons were efficiently collected by PEDOT/Ag electrode. Thus, the charge recombination behaviors can be depicted now. As illustrated in Figure 3e,f, due to the big energy barrier between front cell active layer and PNDIT-F3N modified PEDOT, electrons were inefficiently extracted from front cell to recombine with holes, which resulted in the holes accumulation and S shape curve. However, the energy barrier was largely reduced by the addition of PEI into PNDIT-F3N, therefore, electrons were able to be extracted to recombine with holes, which resulted in an efficient tandem device. Moreover, it was found that due to the n-type semiconducting backbone, PNDIT-F3N can work as both ETL and electron acceptor in OSCs, which enhanced electron collection as well as provided extra current contribution due to charge dissociation between donor in the active layer and PNDIT-F3N.[53–55] To verify if the addition of PEI into PNDIT-F3N hinder the charge dissociation between active layer and PNDIT-F3N, double layer devices with structure ITO/PEDOT/donor materials/PNDIT-F3N:PEI (5:0 and 3:2)/Ag were fabricated, the device without ETL was also included as a comparison. The *J*–*V* curves and device data are shown in Figure S4 and Table S3 of the Supporting Information. It can be seen that the addition of PEI into PNDIT-F3N did not hinder the charge dissociation between donor materials and PNDIT-F3N, which is beneficial for providing extra photocurrent in the tandem OSC. All of these results proved that although PNDIT-F3N was unable to low the WF of PEDOT enough to collect electrons, this problem can be overcome by the addition of PEI. Moreover, the electron transport ability of PNDIT-F3N was not obviously reduced, thus the PNDIT-F3N:PEI combination offered several

distinct advantages, such as water/alcohol solubility and thickness insensitivity, which make it very attractive in printing electronic devices.

Despite efficient tandem OSCs have been realized based on this newly designed ICL, the active layer thickness of both subcells were selected according to the corresponding optimal single junction devices, and had not yet been optimized in tandem devices. Thus there should be still room to further improve the device performance. Optical modeling of the electric field distribution within the OSCs is a powerful mean to predict the optimized structure for the complicated multilayer tandem devices.[11,56,57] Therefore, we performed optical analysis of our tandem OSCs using the transfer matrix modeling method to provide guideline on the best device architecture. According to the simulation result that shown in **Figure 4**a,b, the optimal thicknesses of the front and back cell were 150 and 90 nm, respectively, with maximum J_{sc} of 11.8 mA cm^{-2}. To verify the simulated and experimental results, we fabricated devices with the thickness of the front cell increased from 90 to 150 nm while keeping the back cell thickness to be 100 nm. It can be seen in Figure 4c and **Table 2** that when the thickness of the front cell increased from 90 to 150 nm, the J_{sc} of devices increased apparently from 8.3 to 10.6 mA cm^{-2} although the V_{oc} and FF of tandem solar cell had slightly decreased. This combination resulted in an improved PCE of 12.1% at the optimal conditions. Meanwhile, decreasing the back cell thickness from 100 to 90 nm while keeping the front cell thickness at 150 nm further increased the J_{sc} to 10.8 mA cm^{-2}, leading to a higher PCE of 12.6% (measured to be 13.2% without aperture). These results are in excellent consistence with the simulate results. Notably, these measured results can be verified by the EQE curves of the different subcells. As shown in Figure 4d, the front cell that excited by 850 nm light bias absorbed most of the high-energy photons within the range of 300–700 nm. The integrated J_{sc} of front cell reached to 10.92 mA cm^{-2}. The back cell that excited by 550 nm light bias showed a broad EQE spectrum with a relatively low EQE at the visible range and a high EQE at the infrared range, which corresponded to an integrated J_{sc} of 10.88 mA cm^{-2}. Moreover, EQE measurement with both bias light and bias voltage are also tested and shown in Figure S5 of the Supporting Information. These data show a good consistent with the J_{sc} of the tandem OSC measured under AM 1.5G condition, demonstrating that the measured J_{sc} in our manuscript is reliable. It should be noted that, compare with the reported champion tandem OSC,[27] the slightly lower PCE of our tandem device was resulted from the moderately performed subcells. We believe higher PCE can be obtained if better performed subcells were used. Moreover, the stability of

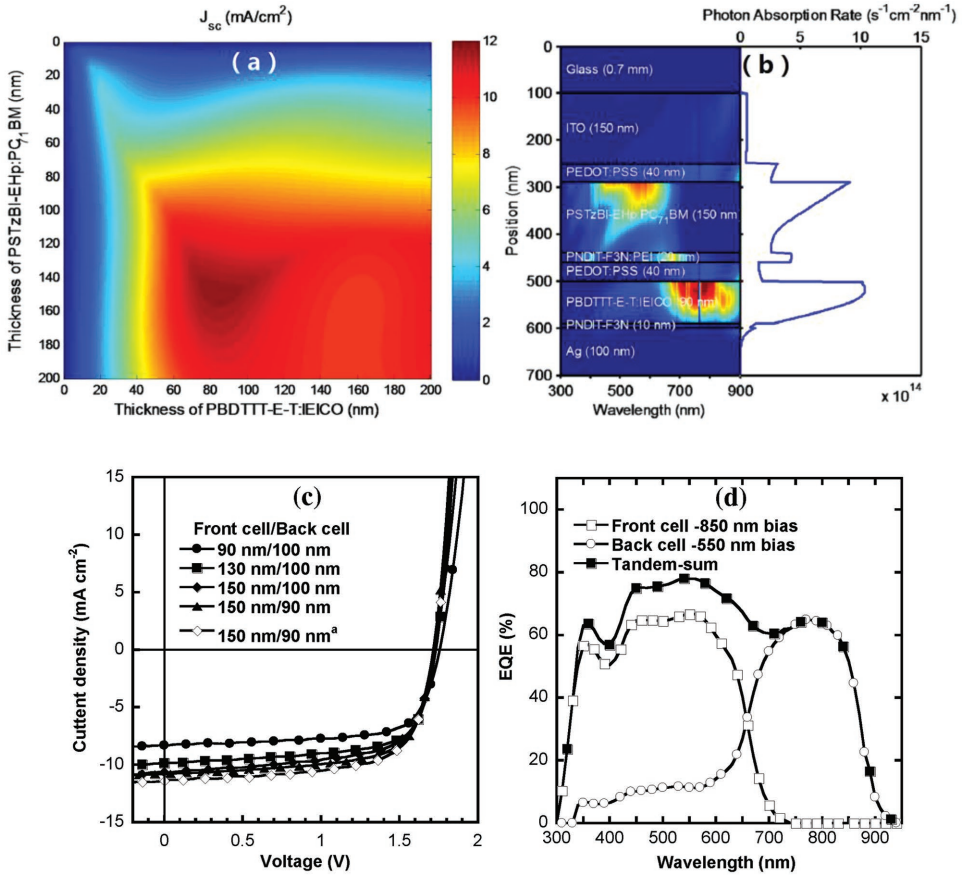

Figure 4. a) Simulated J_{sc} generated in conventional double-junction tandem OSC as a function of thickness of the front and back cells. b) The simulated energy distribution in the optimized tandem OSC with front cell of 150 nm and back cell of 90 nm. c) *J–V* characteristics of tandem OSC with various thicknesses of front and back cells ((a) device was measured without aperture). d) EQE spectra of the front cell, back cell, and summed EQE spectra of the front and back cells.

Table 2. Device data of tandem OSCs with various thicknesses of front cells, back cells, and ICL.

Subcell thickness [nm] Front/back	ICL thickness [nm] ETL/HTL	Simulated J_{sc} [mA cm^{-2}]	Measured J_{sc} [mA cm^{-2}]	Integrated J_{sc} [mA cm^{-2}] Front/back	V_{oc} [V]	FF [%]	PCE[a] (avg/max) [%]
90/100	20/40	9.0	8.3	–	1.75	70	9.9 ± 0.3 (10.2)
130/100	20/40	11.1	9.9	–	1.73	69	11.4 ± 0.3 (11.7)
150/100	20/40	11.5	10.6	–	1.72	66	11.9 ± 0.2 (12.1)
150/90	20/40	11.8	10.8	10.92/10.88	1.72	68	12.3 ± 0.3 (12.6)
150/90[b]	20/40	–	11.4	–	1.72	67	12.9 ± 0.3 (13.2)
150/90	40/40	–	10.7	–	1.72	68	12.2 ± 0.3 (12.5)
150/90	70/40	–	10.2	–	1.72	66	11.2 ± 0.2 (11.4)
150/90	70/70	–	10.1	–	1.72	65	11.1 ± 0.2 (11.3)

[a]The average data were achieved from ten independent devices; [b]The device was measured without aperture with device area of 5.16 mm^2.

tandem solar cell together with both single junction front cell and back cell were tested. As shown in Figure S6 of the Supporting Information, the single junction front cell and back cell retained 91% and 94% of their initial PCE after 12 d storage, while the tandem device exhibited better stability with PCE of 12.1% (96% of its initial PCE) after 12 d storage, implying that tandem device has a good stability. To further test the universality of this ICL in other OSC system, we have applied the ICL in PTB7-Th:$PC_{71}BM$-based homojunction tandem device. These results are shown in Table S4 of the Supporting Information. It can be seen that this ICL can drive the PCE of homojunction tandem device close to 11%, which is much higher than the single junction device, demonstrating a good universality of this ICL in other OSC system.

Since PNDIT-F3N provides the matrix for electron transport, while the addition of PEI does not decrease the conductivity of PNDIT-F3N apparently, which indicates that the PNDIT-F3N:PEI (3:2) can also exhibit an excellent performance within a wide range of thicknesses. The dependence of tandem OSC performance on ICL thickness is tested. As shown in **Figure 5** and Table 2, when the thickness of PNDIT-F3N:PEI (3:2) increased from 20 to 70 nm, the PCE decreased slightly from 12.6% to 11.4% as a result of the slightly decreased J_{sc} from 10.8 to 10.2 mA cm^{-2}, while the V_{oc} and FF of tandem OSCs remained almost unchanged. This can be ascribed to the excellent charge transport ability of PNDIT-F3N. Further increasing the thickness of PEDOT to 70 nm (with ICL total thickness of 140 nm) resulted in an impressive PCE of 11.3%. This feature is very important since it offers this ICL the opportunity to be printed even with a large thickness variation, exhibiting great potential for the application in large area module device fabrication.

In summary, a new ICL configuration based on PNDIT-F3N:PEI/PEDOT:PSS was developed and applied for the fabrication of high performance tandem OSCs. It was found that the WF modification ability of PNDIT-F3N on PEDOT can be linearly tuned by the incorporation of PEI. The optimized PNDIT-F3N:PEI (3:2)/PEDOT blend can form Ohmic contact with both subcells in the tandem OSCs and also protect the front cell from being destroyed by back cell solution. Tandem OSCs employing this ICL achieved a high PCE of 12.6% with ICL thickness of 60 nm and even reached to 11.3% with ICL thickness of 140 nm.

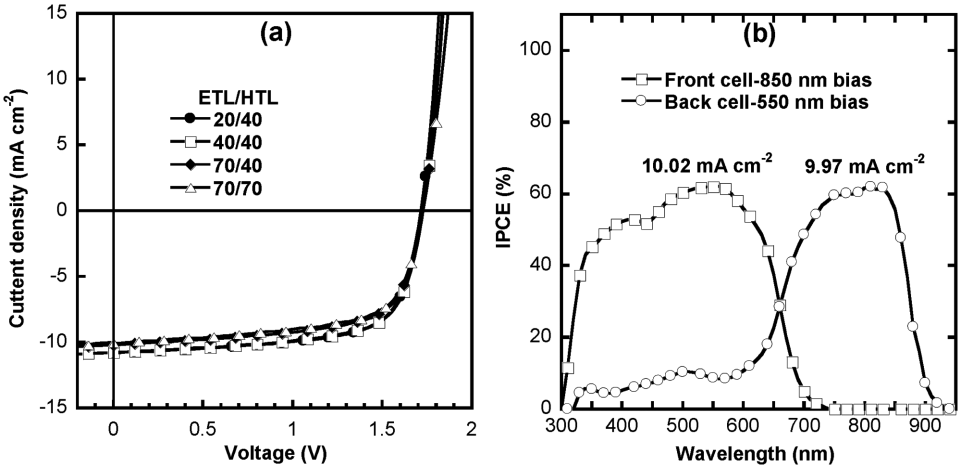

Figure 5. a) *J–V* characteristics of tandem OSCs with various thickness of ICL and b) EQE spectra of the front cell and back cell with ICL thickness of 70/70 nm, where the thickness of front cell and back cell were 150 and 90 nm.

This result is comparable to tandem OSCs with inorganic metal oxides ICL, and offers a new selection for constructing efficient ICL in high performance tandem OSCs. Our results provide a new guideline of design new ETL materials for ICL construction, and may even be integrated in future printed flexible large area module device fabrication with the advantages of environmentally friendly solvent processing and thickness insensitivity.

Experimental Section

Single-Junction OSC Fabrication: ITO-coated glass substrates were rinsed with standard procedure. The single-junction cells of the PSTzBI-EHp:$PC_{71}BM$ and PBDTTT-E-T:IEICO were fabricated according to previously reports[45,46] except that PNDIT-F3N was used as the cathode interlayer and Ag (100 nm) was used as the cathode. The PNDIT-F3N was spin-coated from MeOH solution to achieve a film of 10 nm. The equivalent devices were fabricated with the same procedure as single-junction device except that PEDOT was spin-coated onto ETL before the deposition of Ag electrode.

Tandem OSC Fabrication: 40 nm PEDOT:PSS (Clevios P VP AI4083) was spin-coated onto ITO substrates and baked at 150 °C for 20 min. Then, PSTzBI-EHp:$PC_{71}BM$ active layers (1:1 w/w) were spin-coated from its dichlorobenzene solution onto PEDOT:PSS to achieve films with thickness of 90–150 nm and baked at 120 °C for 10 min in a nitrogen protected glove box. PNDIT-F3N:PEI with different blend ratio were spin-coated onto PSTzBI-EHp:$PC_{71}BM$ by varying the concentration and spin-coat speed to achieve different thicknesses. After that, PEDOT:PSS was spin-coated onto the PNDIT-F3N:PEI blend film in ambient atmosphere and stored in low vacuum (10^0 Pa) for 30 min to remove the residual water. Then, 90–100 nm PBDTTT-E-T:IEICO active layer were spin-coated onto PEDOT:PSS from its mixed solvent of chlorobenzene/1,8-diiodooctane (100:2 v/v) solution and baked at 100 °C for 10 min to complete the thermal annealing process. Subsequently, 10 nm PNDIT-F3N was spin-coated onto PBDTTT-E-T:IEICO. Devices were at last finished by evaporating 100 nm Ag through a shadow mask (5.16 mm^2) in a vacuum chamber with a base pressure of 1×10^{-7} Torr.

Device Characterization: The *J–V* curves were measured on a computer-controlled Keithley 2400 sourcemeter under 1 sun, AM 1.5 G spectra from a class solar simulator (Taiwan, Enlitech), the light intensity was 100 mW cm^{-2} as calibrated by a China general certification center certified reference monocrystal silicon cell (Enlitech). Before the *J–V* test, a physical mask of an aperture with precise area of 4 mm^2 was used to define the device area. The EQE spectra were performed on a commercial EQE measurement system (Taiwan, Enlitech, QE-R3011). Light biases of 550 and 850 nm were selected to excite the front and back subcells in the tandem devices.

Optical Modeling: The optical model was preformed based on the transfer matrix formalism. The optical parameters, *n* and *k,* of the different films were measured using a dual rotating-compensator Mueller matrix ellipsometer (ME-L ellipsometer, Wuhan Eoptics Technology Co., Wuhan, China). More detail description of the modeling and fitting methods for the optical parameters is provided in the Supporting Information.

Supporting Information

Supporting Information is available from the Wiley Online Library or from the author.

Acknowledgements

The work was financially supported by the Natural Science Foundation of China (Nos. 21634004, 51521002, and 91633301) and the Ministry of Science and Technology (No. 2014CB643501), Science and Technology Program of Guangzhou (No. 201707020019). K.Z. thanks the National Natural Science Foundation of China (No.51603070) and China Postdoctoral Science Foundation (2017T100626) for financial support.

Conflict of Interest

The authors declare no conflict of interest.

Keywords

charge recombination, environmentally friendly, polymeric interconnecting layers, tandem organic solar cells, thickness insensitive

Received: November 13, 2017
Revised: January 2, 2018
Published online: February 12, 2018

[1] G. Yu, J. Gao, J. C. Hummelen, F. Wudl, A. J. Heeger, *Science* **1995**, *270*, 1789.
[2] B. Kippelen, J.-L. Bredas, *Energy Environ. Sci.* **2009**, *2*, 251.
[3] C. J. Brabec, S. Gowrisanker, J. J. M. Halls, D. Laird, S. Jia, S. P. Williams, *Adv. Mater.* **2010**, *22*, 3839.
[4] R. Søndergaard, M. Hösel, D. Angmo, T. T. Larsen-Olsen, F. C. Krebs, *Mater. Today* **2012**, *15*, 36.
[5] Y. Liu, J. Zhao, Z. Li, C. Mu, W. Ma, H. Hu, K. Jiang, H. Lin, H. Ade, H. Yan, *Nat. Commun.* **2014**, *5*, 5293.
[6] Y. Jin, Z. Chen, S. Dong, N. Zheng, L. Ying, X.-F. Jiang, F. Liu, F. Huang, Y. Cao, *Adv. Mater.* **2016**, *28*, 9811.
[7] W. Zhao, D. Qian, S. Zhang, S. Li, O. Inganäs, F. Gao, J. Hou, *Adv. Mater.* **2016**, *28*, 4734.
[8] W. Zhao, S. Li, H. Yao, S. Zhang, Y. Zhang, B. Yang, J. Hou, *J. Am. Chem. Soc.* **2017**, *139*, 7148.
[9] D. Liu, Q. Zhu, C. Gu, J. Wang, M. Qiu, W. Chen, X. Bao, M. Sun, R. Yang, *Adv. Mater.* **2016**, *28*, 8490.
[10] K. Zhang, F. Huang, Y. Cao, *Acta Polym. Sin.* **2017**, *9*, 1400.
[11] N.-K. Persson, O. Inganäs, *Sol. Energy Mater. Sol. Cells* **2006**, *90*, 3491.
[12] J. Y. Kim, K. Lee, N. E. Coates, D. Moses, T.-Q. Nguyen, M. Dante, A. J. Heeger, *Science* **2007**, *317*, 222.
[13] G. Dennler, M. C. Scharber, T. Ameri, P. Denk, K. Forberich, C. Waldauf, C. J. Brabec, *Adv. Mater.* **2008**, *20*, 579.
[14] L. Zuo, C.-Y. Chang, C.-C. Chueh, S. Zhang, H. Li, A. K. Y. Jen, H. Chen, *Energy Environ. Sci.* **2015**, *8*, 1712.
[15] A. Hadipour, B. de Boer, P. W. M. Blom, *Org. Electron.* **2008**, *9*, 617.
[16] T. Ameri, N. Li, C. J. Brabec, *Energy Environ. Sci.* **2013**, *6*, 2390.
[17] W. Li, A. Furlan, K. H. Hendriks, M. M. Wienk, R. A. J. Janssen, *J. Am. Chem. Soc.* **2013**, *135*, 5529.
[18] A. Hadipour, B. de Boer, P. W. M. Blom, *Adv. Funct. Mater.* **2008**, *18*, 169.
[19] D. Gupta, M. Bag, K. S. Narayan, *Appl. Phys. Lett.* **2008**, *93*, 163301.
[20] A. Armin, M. Hambsch, P. Wolfer, H. Jin, J. Li, Z. Shi, P. L. Burn, P. Meredith, *Adv. Energy Mater.* **2015**, *5*, 1401221.
[21] L. Mao, J. Tong, S. Xiong, F. Jiang, F. Qin, W. Meng, B. Luo, Y. Liu, Z. Li, Y. Jiang, C. Fuentes-Hernandez, B. Kippelen, Y. Zhou, *J. Mater. Chem. A.* **2017**, *5*, 3186.
[22] K. Zhang, Z. Chen, A. Armin, S. Dong, R. Xia, H.-L. Yip, S. Shoaee, F. Huang, Y. Cao, *Solar RRL* **2017**, *2*, 1700169.
[23] J. You, L. Dou, Z. Hong, G. Li, Y. Yang, *Prog. Polym. Sci.* **2013**, *38*, 1909.

[24] G. Li, W.-H. Chang, Y. Yang, *Nat. Rev. Mater.* **2017**, *2*, 17043.
[25] P. Boland, K. Lee, J. Dean, G. Namkoong, *Sol. Energy Mater. Sol. Cells* **2010**, *94*, 2170.
[26] Y. Qin, Y. Chen, Y. Cui, S. Zhang, H. Yao, J. Huang, W. Li, Z. Zheng, J. Hou, *Adv. Mater.* **2017**, *29*, 1606340.
[27] Y. Cui, H. Yao, B. Gao, Y. Qin, S. Zhang, B. Yang, C. He, B. Xu, J. Hou, *J. Am. Chem. Soc.* **2017**, *139*, 7302.
[28] J. W. Shim, Y. Zhou, C. Fuentes-Hernandez, A. Dindar, Z. Guan, H. Cheun, A. Kahn, B. Kippelen, *Sol. Energy Mater. Sol. Cells* **2012**, *107*, 51.
[29] J. Yang, W. Chen, B. Yu, H. Wang, D. Yan, *Org, Electron.* **2012**, *13*, 1018.
[30] M. Vasilopoulou, E. Polydorou, A. M. Douvas, L. C. Palilis, S. Kennou, P. Argitis, *Energy Environ. Sci.* **2015**, *8*, 2448.
[31] J. Yang, R. Zhu, Z. Hong, Y. He, A. Kumar, Y. Li, Y. Yang, *Adv. Mater.* **2011**, *23*, 3465.
[32] T. R. Andersen, H. F. Dam, M. Hosel, M. Helgesen, J. E. Carle, T. T. Larsen-Olsen, S. A. Gevorgyan, J. W. Andreasen, J. Adams, N. Li, F. Machui, G. D. Spyropoulos, T. Ameri, N. Lemaitre, M. Legros, A. Scheel, D. Gaiser, K. Kreul, S. Berny, O. R. Lozman, S. Nordman, M. Valimaki, M. Vilkman, R. R. Sondergaard, M. Jorgensen, C. J. Brabec, F. C. Krebs, *Energy Environ. Sci.* **2014**, *7*, 2925.
[33] F. Guo, N. Li, V. V. Radmilovic, V. R. Radmilovic, M. Turbiez, E. Spiecker, K. Forberich, C. J. Brabec, *Energy Environ. Sci.* **2015**, *8*, 1690.
[34] S. Lu, D. Ouyang, W. C. H. Choy, *Sci. China Chem.* **2017**, *60*, 460.
[35] J. You, L. Dou, K. Yoshimura, T. Kato, K. Ohya, T. Moriarty, K. Emery, C.-C. Chen, J. Gao, G. Li, Y. Yang, *Nat. Commun.* **2013**, *4*, 1446.
[36] S. Chen, G. Zhang, J. Liu, H. Yao, J. Zhang, T. Ma, Z. Li, H. Yan, *Adv. Mater.* **2017**, *29*, 1604231.
[37] M. Li, K. Gao, X. Wan, Q. Zhang, B. Kan, R. Xia, F. Liu, X. Yang, H. Feng, W. Ni, Y. Wang, J. Peng, H. Zhang, Z. Liang, H.-L. Yip, X. Peng, Y. Cao, Y. Chen, *Nat. Photonics* **2017**, *11*, 85.
[38] H. Zhou, Y. Zhang, C.-K. Mai, S. D. Collins, G. C. Bazan, T.-Q. Nguyen, A. J. Heeger, *Adv. Mater.* **2015**, *27*, 1767.
[39] J. Gilot, M. M. Wienk, R. A. J. Janssen, *Appl. Phys. Lett.* **2007**, *90*, 143512.
[40] S. Lu, X. Guan, X. Li, J. Liu, F. Huang, W. C. H. Choy, *Nano Energy* **2016**, *21*, 123.
[41] Y. Zhou, C. Fuentes-Hernandez, J. W. Shim, T. M. Khan, B. Kippelen, *Energy Environ. Sci.* **2012**, *5*, 9827.
[42] A. R. b. M. Yusoff, S. J. Lee, H. P. Kim, F. K. Shneider, W. J. da Silva, J. Jang, *Adv. Funct. Mater.* **2014**, *24*, 2240.
[43] Y. Liu, C.-C. Chen, Z. Hong, J. Gao, Y. Yang, H. Zhou, L. Dou, G. Li, Y. Yang, *Sci. Rep.* **2013**, *3*, 3356.
[44] C.-Y. Chang, W.-K. Huang, Y.-C. Chang, K.-T. Lee, H.-Y. Siao, *Chem. Mater.* **2015**, *27*, 1869.
[45] L. Lan, Z. Chen, Q. Hu, L. Ying, R. Zhu, F. Liu, T. P. Russell, F. Huang, Y. Cao, *Adv. Sci.* **2016**, *3*, 1600032.
[46] H. Yao, Y. Chen, Y. Qin, R. Yu, Y. Cui, B. Yang, S. Li, K. Zhang, J. Hou, *Adv. Mater.* **2016**, *28*, 8283.
[47] S. Foster, F. Deledalle, A. Mitani, T. Kimura, K.-B. Kim, T. Okachi, T. Kirchartz, J. Oguma, K. Miyake, J. R. Durrant, S. Doi, J. Nelson, *Adv. Energy Mater.* **2014**, *4*, 1400311.
[48] Z. Wu, C. Sun, S. Dong, X.-F. Jiang, S. Wu, H. Wu, H.-L. Yip, F. Huang, Y. Cao, *J. Am. Chem. Soc.* **2016**, *138*, 2004.
[49] C. Sun, Z. Wu, H.-L. Yip, H. Zhang, X.-F. Jiang, Q. Xue, Z. Hu, Z. Hu, Y. Shen, M. Wang, F. Huang, Y. Cao, *Adv. Energy Mater.* **2016**, *6*, 1501534.
[50] Y. Zhou, C. Fuentes-Hernandez, J. Shim, J. Meyer, A. J. Giordano, H. Li, P. Winget, T. Papadopoulos, H. Cheun, J. Kim, M. Fenoll, A. Dindar, W. Haske, E. Najafabadi, T. M. Khan, H. Sojoudi, S. Barlow, S. Graham, J.-L. Brédas, S. R. Marder, A. Kahn, B. Kippelen, *Science* **2012**, *336*, 327.
[51] S. van Reenen, S. Kouijzer, R. A. J. Janssen, M. M. Wienk, M. Kemerink, *Adv. Mater. Interfaces* **2014**, *1*, 1400189.
[52] B. H. Lee, I. H. Jung, H. Y. Woo, H.-K. Shim, G. Kim, K. Lee, *Adv. Funct. Mater.* **2014**, *24*, 1100.
[53] C. Sun, Z. Wu, Z. Hu, J. Xiao, W. Zhao, H.-W. Li, Q.-Y. Li, S. W. Tsang, Y.-X. Xu, K. Zhang, H.-L. Yip, J. Hou, F. Huang, Y. Cao, *Energy Environ. Sci.* **2017**, *10*, 1784.
[54] H. Shi, R. Xia, C. Sun, J. Xiao, Z. Wu, F. Huang, H.-L. Yip, Y. Cao, *Adv. Energy Mater.* **2017**, *7*, 1701121.
[55] S. Dong, Z. Hu, K. Zhang, Q. Yin, X. Jiang, F. Huang, Y. Cao, *Adv. Mater.* **2017**, *29*, 1701507.
[56] A. R. b. M. Yusoff, D. Kim, H. P. Kim, F. K. Shneider, W. J. da Silva, J. Jang, *Energy Environ. Sci.* **2015**, *8*, 303.
[57] C.-C. Chen, W.-H. Chang, K. Yoshimura, K. Ohya, J. You, J. Gao, Z. Hong, Y. Yang, *Adv. Mater.* **2014**, *26*, 5670.

ADVANCED ENERGY MATERIALS

Supporting Information

for *Adv. Energy Mater.,* DOI: 10.1002/aenm.201703180

Highly Efficient Tandem Organic Solar Cell Enabled by Environmentally Friendly Solvent Processed Polymeric Interconnecting Layer

Kai Zhang, Baobing Fan, Ruoxi Xia, Xiang Liu, Zhicheng Hu, Honggang Gu, Shiyuan Liu, Hin-Lap Yip, Lei Ying, Fei Huang,* and Yong Cao*

Supporting Information

Highly Efficient Tandem Organic Solar Cell Enabled by Environmentally-friendly Solvent Processed Polymeric Interconnecting Layer

Kai Zhang, Baobing Fan, Ruoxi Xia, Xiang Liu, Zhicheng Hu, Honggang Gu, Shiyuan Liu, Hin-Lap Yip, Lei Ying*, Fei Huang* and Yong Cao

Dr. K. Zhang, B. Fan, R. Xia, X. Liu, Dr. Z. Hu, Prof. H.-L. Yip, Prof. L. Ying, Prof. F. Huang, Prof. Y. Cao
Institute of Polymer Optoelectronic Materials and Devices, State Key Laboratory of Luminescent Materials and Devices, South China University of Technology, Guangzhou 510640, P. R. China.
E-mail: msleiying@scut.edu.cn; msfhuang@scut.edu.cn.
Dr. H. Gu, Prof. S. Liu
State Key Laboratory of Digital Manufacturing Equipment and Technology, Huazhong University of Science and Technology, Wuhan 430074, P. R. China.

Materials: PEI and $PC_{71}BM$ were purchased from Aldrich and used as received. PBDTTT-E-T and IEICO were purchased from Solarmer Materials (Beijing) and used as received. PNDIT-F3N was synthesized according to our previous work.[1] The synthesis route of PSTzBI-EHp are as follows:

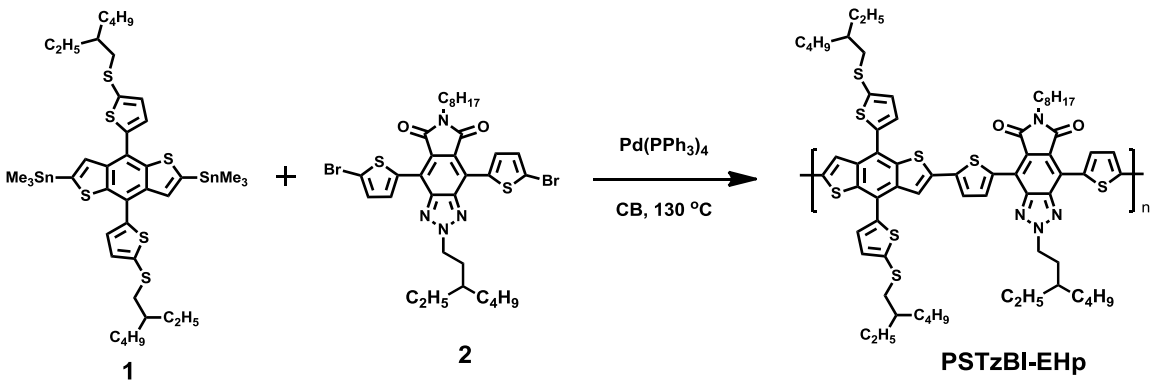

(4,8-Bis(5-((2-ethylhexyl)thio)thiophen-2-yl)benzo[1,2-b:4,5-b']dithiophene-2,6-diyl) bis(trimethylstannane) (**1**) and 4,8-bis(5-bromothiophen-2-yl)-2-(3-ethylheptyl)-6-octyl-[1,2,3]triazolo[4,5-f]isoindole-5,7(2H,6H)-dione (**2**) were prepared according to the reported methods.[2, 3] (4,8-Bis(5-((2-ethylhexyl)thio)thiophen-2-yl)benzo[1,2-b:4,5-b']dithiophene-2,6-diyl) bis(trimethylstannane) (**1**, 0.1 mmol, 97.0 mg), 4,8-bis(5-bromothiophen-2-yl)-2-(3-ethylheptyl)-6-octyl-[1,2,3]triazolo[4,5-f]isoindole-5,7(2H,6H)-dione (**2**, 0.1 mmol, 74.6 mg), and 2 mL dry chlorobenzene were combined in a 15 mL pressure pipe and purged with argon for 15 min. After 6 mg $Pd_2(PPh_3)_4$ was quick added， the pressure pipe was sealed and the mixture was stirred at 130 ^oC in oil bath for 48 h. After cooled to room temperature, the dark purple mixture was precipitated into 250 mL methanol by a glass dropper. The obtained solid was filtered and extracted with methane, acetone, hexane, and chloroform. The chloroform ingredient was concentrated, precipitated again into 250 mL methanol, filtered and dried under vacuum to give the final polymer. Yield: 83.4%.

n, k value measurement: At first, thin films with thickness of about 100 nm are manufactured by depositing the studied materials on the ITO glass. Dual rotating-compensator Mueller matrix ellipsometer (ME-L ellipsometer, Wuhan Eoptics Technology Co., Wuhan, China)[4] was used to collect the ellipsometric data of the thin film samples. The layout of the MME in order of light propagation is PCr1SCr2A, where P and A stand for the polarizer and analyzer, Cr1 and Cr2 refer to the 1st and 2nd rotating compensators, and S stands for the sample. With this dual rotating-compensator configuration, the full Mueller matrix elements can be obtained in a single measurement. The spectral range is from 200 nm to 1000 nm. The beam

diameter can be changed from the normal value of about 3 mm to a value less than 200 μm with the focusing lens. The two arms of the instrument and the sample stage can be rotated to change the incidence angle and azimuthal angle in the experiments. And then, the optical constant of the studied materials as well as the film thickness can be extracted from the measured ellipsometric data, by performing a weighted least-squares regression analysis method (Levenberg-Marquardt algorithm)[5]. In the data analysis, the optical constant of the ITO film as well as the glass are determined by performing a measurement on a blank ITO coated film. And the optical constant of the studied materials can be characterized by superimposing the general oscillator models (such as Lorentz model,[6] Tauc-Lorentz model,[7] Gaussian model[8] etc.), which can characterize simple materials. This is done by linearly adding the general oscillator models to the polo model, which is a zero-broadening oscillator.

In our experiment, in order to achieve a high accuracy result, the incident angle is set to be 55° to 65° by 5° to eliminate the effect of data coupling. The spectral range is 300 nm to 1000 nm by 1nm.

Optical modeling: In the series structure, voltage is the sum of each sub cell but current is limited by the minimum one of all sub-cells in theory. To deal with this ‘‘Cask Effect’’ of short circuit current density (J_{sc}), thicknesses of the BHJ layers should be optimized in order to achieve a balanced and high J_{sc}. The optical model based on Transfer Matrix Formalism (TMF) can simplify the optimization design and predict the performance of device with certain structure.

The TMF method analyzes the propagation of light incident on stacks of layers. This theory assumes that all layers are homogeneous and their interfaces are flat and parallel so that each layer can just be described by its thickness and optical parameter N which is so-called complex refractive index and all of these parameters can be determined by spectroscopic ellipsometry. In addition, the incidence light should be described by plane waves. Based on these aforementioned assumptions, light propagation in medium or at interface can be skillfully described by matrices due to the linearity and continuity of electric field component. TMF takes account of the effects of light wave character and reflection and transmission at medium interfaces so it can give a precise description of light propagation in layer stacks.

Optical model can utilize TMF to calculate the optical electric field intensity (|E|) at each position of the whole multilayer structure. Then we can use the relationship between |E| and absorption strength to obtain the distribution of energy. After integrating the absorbed energy in each BHJ layer, we can get J_{sc} of each sub-cell and the smallest one represents the whole device's J_{sc}. Because the model just considers the optics aspect, the J_{sc} is an ideal value based on the 100-percent IQE, that is, all absorbed photons are contributing to the steady state photocurrent.

We can get J_{sc}s of devices with different thicknesses of BHJ layers by optical model and then easily find the optimal design.

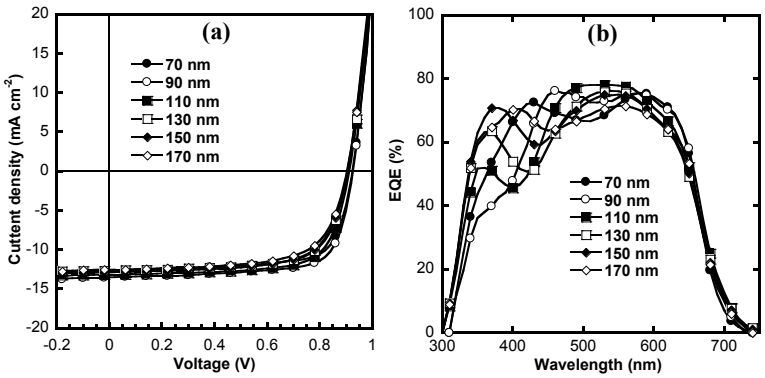

Figure S1. a) *J-V* and b) EQE characteristics of wide-bandgap active layer with thickness varied from 70 nm to 170 nm.

Table S1. Device performances of wide-bandgap active layer and narrow-bandgap active layer in single junction cells.

Active layer	Thickness (nm)	Measured J_{sc} (mA cm^{-2})	Integrated J_{sc} (mA cm^{-2})	V_{oc} (V)	FF (%)	PCE (avg[a]/max) (%)
PSTzBI-EHp:$PC_{71}BM$	70	12.8	12.5	0.93	72	8.6±0.1(8.7)
	90	13.5	13.1	0.93	73	9.0±0.2(9.2)
	110	13.2	12.7	0.92	72	8.5±0.2(8.7)
	130	12.8	12.5	0.91	70	8.1±0.2(8.3)
	150	12.9	12.5	0.90	69	7.7±0.3(8.0)
	170	12.5	12.3	0.90	67	7.4±0.2(7.6)
PBDTTT-E-T:IEICO	100	17.5	17.3	0.82	67	9.4±0.2(9.6)

[a)]The average data were achieved from 10 independent devices.

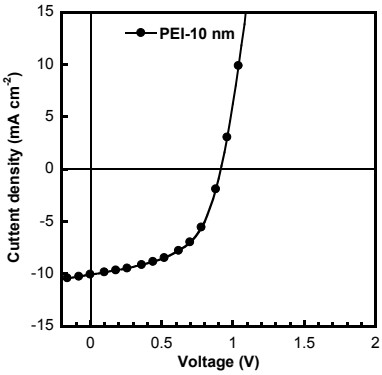

Figure S2. *J-V* characteristics of tandem OSC with ICL containing 10 PEI as ETL.

Table S2. Work function of PEDOT and Ag coated with different ratio of PNDIT-F3N:PEI

Substrate	WF (eV)	Substrate	WF (eV)
PEDOT	4.98	Ag	4.59
PEDOT/PNDIT-F3N:PEI (5:0)	4.43	Ag/PNDIT-F3N(5:0)	4.04
PEDOT/PNDIT-F3N:PEI (4:1)	4.30		
PEDOT/PNDIT-F3N:PEI (3:2)	4.13		
PEDOT/PNDIT-F3N:PEI (2:3)	4.01		
PEDOT/PNDIT-F3N:PEI (1:4)	3.89		
PEDOT/PNDIT-F3N:PEI (0:5)	3.75		

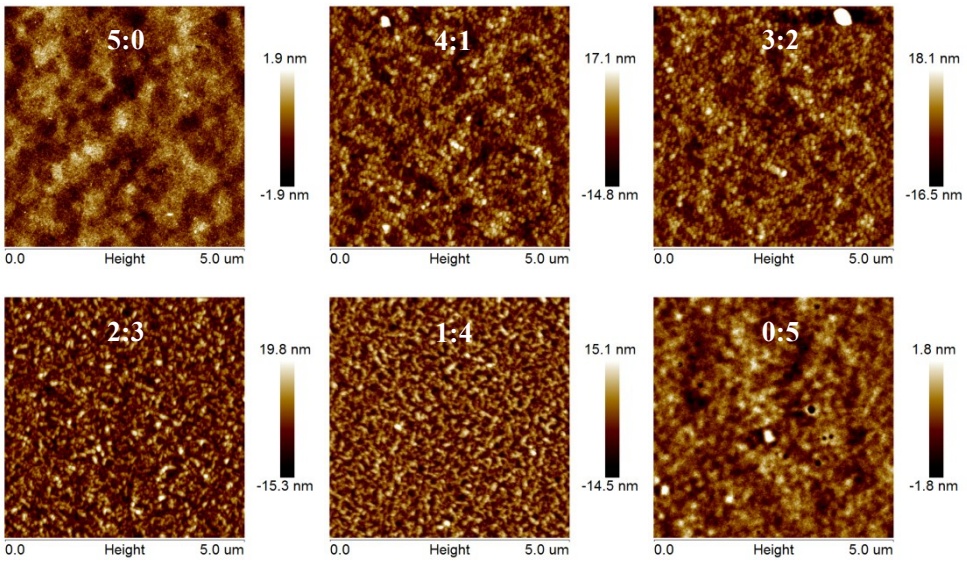

Figure S3. AFM images of PNDIT-F3N:PEI films with different blend ratios.

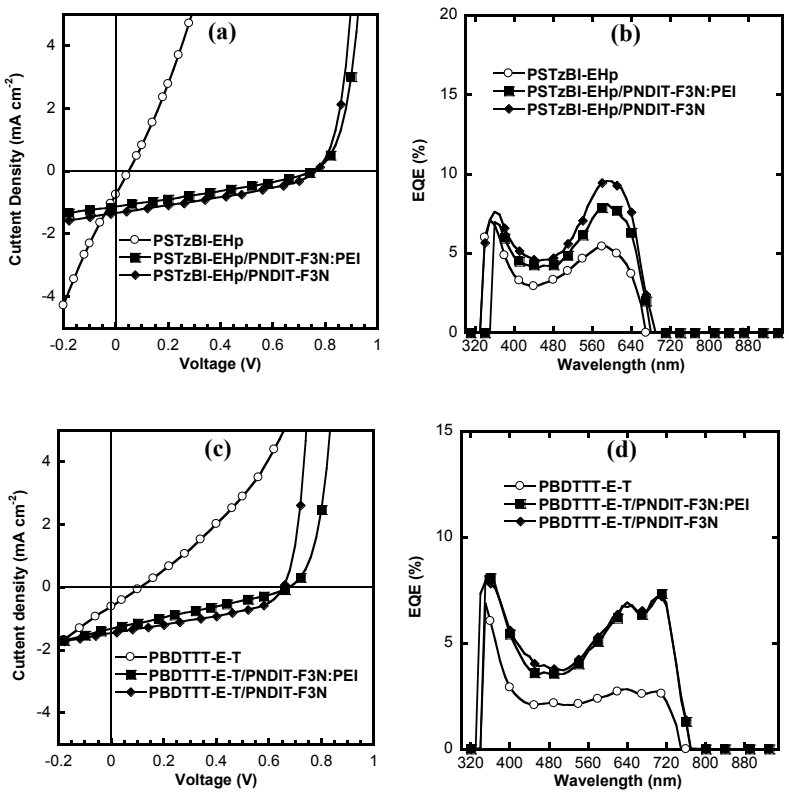

Figure S4. a) *J-V* and b) EQE characteristics of bilayer devices based on PSTzBI-EHp/PNDIT-F3N:PEI. c) *J-V* and d) EQE characteristics of bilayer devices based on PBDTTT-E-T/PNDIT-F3N:PEI.

Table S3. Device data based on PSTzBI-EHp/PNDIT-F3N:PEI and PBDTTT-E-T/PNDIT-F3N:PEI.

Donor	ETL (acceptor)	Mea. J_{sc} (mA cm^{-2})	Cal. Jsc (mA cm^{-2})	V_{oc} (V)	FF (%)	PCE (%)
PSTzBI-EHp	NO	0.74	0.68	0.05	25	0.01
	PNDIT-F3N	1.33	1.23	0.76	35	0.35
	PNDIT-F3N:PEI (3:2)	1.12	1.03	0.75	30	0.25
PBDTTT-E-T	NO	0.61	0.57	0.11	26	0.02
	PNDIT-F3N	1.45	1.33	0.65	39	0.37
	PNDIT-F3N:PEI (3:2)	1.32	1.26	0.68	28	0.25

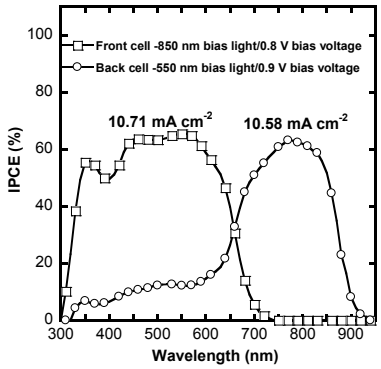

Figure S5. EQE spectra of the front cell and back cell with both bias light and bias voltage.

Table S4. Performance of PTB7-Th:$PC_{71}BM$ based single junction device and homo-junction tandem device

	J_{sc} (mA cm^{-2})	V_{oc} (V)	FF (%)	PCE (avg[a]/max) (%)
Single junction	16.8	0.78	73	9.6±0.1(9.7)
tandem	9.6	1.56	72	10.7±0.2(10.9)

[a)]The average data were achieved from 10 independent devices.

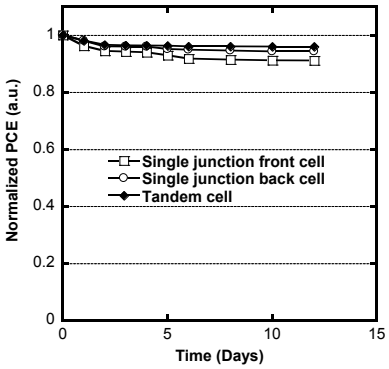

Figure S6. Average device PCE versus storage time with devices were stored in N_2 protected glove box without encapsulation. Average data were obtained from 8 independent devices.

Reference

[1] Z. Wu, C. Sun, S. Dong, X.-F. Jiang, S. Wu, H. Wu, H.-L. Yip, F. Huang, Y. Cao, *J. Am. Chem. Soc.* **2016**, *138*, 2004.

[2] H. Bin, Z. G. Zhang, L. Gao, S. Chen, L. Zhong, L. Xue, C. Yang, Y. Li, *J. Am. Chem. Soc.* **2016**, *138*, 4657.

[3] L. Lan, Z. Chen, Q. Hu, L. Ying, R. Zhu, F. Liu, T. P. Russell, F. Huang, Y. Cao, *Adv. Sci.* **2016**, *3*, 1600032.

[4] S. Liu, X. Chen, C. Zhang, *Thin Solid Films* **2015**, *584*, 176.

[5] W. H. Press, S. A. Teukolsky, W. T. Vetterling, B. P. Flannery, Numerical Recipes: The Art of Scientific Computing, 3rd ed. (Cambridge University Press, Cambridge, **2007**)

[6] H. Fujiwara, Spectroscopic Ellipsometry: Principles and Applications (John Wiley & Sons, **2007**).

[7] G. E. Jellison Jr. and F. A. Modine, *App. Phys. Lett.* **1996**, *69*, 371.

[8] T. E. Tiwald, D. W. Thompson, J. A. Woollam, W. Paulson, R. Hance, *Thin Solid Films*, **1998**, *313*, 661.